

How thermal fluctuations affect hard-wall repulsion and thereby Hertzian contact mechanics

Yunong Zhou, Anle Wang, and Martin H. Müser

Lehrstuhl für Materialsimulation, Dept. of Materials Science and Engineering, Saarland University, 66123 Saarbrücken, Germany

Correspondence*:

Martin H. M^user

martin.mueser@mx.uni-saarland.de

2 ABSTRACT

3 Contact problems as they occur in tribology and colloid science are often solved with
4 the assumption of hard-wall and hard-disk repulsion between locally smooth surfaces. This
5 approximation is certainly meaningful at sufficiently coarse scales. However, at small scales,
6 thermal fluctuations can become relevant. In this study, we address the question how they render
7 non-overlap constraints into finite-range repulsion. To this end, we derive a closed-form analytical
8 expression for the potential of mean force between a hard wall and a thermally fluctuating, linearly
9 elastic counterface. Theoretical results are validated with numerical simulations based on the
10 Green's function molecular dynamics technique, which is generalized to include thermal noise
11 while allowing for hard-wall interactions. Applications consist of the validation of our method
12 for flat surfaces and the generalization of the Hertzian contact to finite temperature. In both
13 cases, similar force-distance relationships are produced with effective potentials as with fully
14 thermostatted simulations. Analytical expressions are identified that allow the thermal corrections
15 to the Hertzian load-displacement relation to be accurately estimated. While these corrections
16 are not necessarily small, they turn out surprisingly insensitive to the applied load.

1 INTRODUCTION

17 One of several drawbacks when applying continuum theory to small-scale contact problems, as they occur,
18 for example, in contact mechanics or in colloid science, is that continuum theories often ignore the effect
19 of thermal fluctuations. This can lead to noticeable errors of continuum-theory based predictions for the
20 dependence of displacement or indentation on load when two objects are pressed against each other [1, 2].
21 Temperature can affect mechanical contacts and their interpretation in numerous other ways. For example,
22 the presence of thermal noise generally impedes an unambiguous definition of contact area [3, 4, 5, 6, 7]. In
23 addition, large standard deviations of experimentally measured depinning forces of atomic-force microscope
24 tips have been observed, which were accompanied by unexpectedly large reductions of the depinning force
25 with increasing temperature [8]. It is possible that thermal surface fluctuations, which were not included
26 in the modeling of temperature effects on tip depinning, are responsible for a significant reduction of
27 effective surface energy and thereby for a reduction of the depinning force. In fact, it has been shown that
28 thermal fluctuations limit the adhesive strength of compliant solids [9]. Finally, in the context of colloid
29 science, it may well be that thermal corrections have a non-negligible effect on the surprisingly complex

30 phase diagram of Hertzian spheres [10]. It is therefore certainly desirable to model the effect of thermal
31 fluctuations in a variety of contact and colloid problems.

32 While thermal fluctuations can be incorporated into simulations with so-called thermostats [11, 12],
33 proper sampling can require a significant computational overhead. In addition, some contact solvers do not
34 appear amenable to thermostating. This concerns in particular those contact-mechanics approaches that
35 optimize the stress field, as done with the classical solver by Polonsky and Keer [13, 14], rather than the
36 displacement fields as done with the Green's function molecular dynamics (GFMD) method [15, 16].

37 The just-mentioned issues motivated us to investigate how thermal noise affects the mean force F (per
38 unit area) between surfaces as a function of their interfacial separation, or, gap g . The pursued idea is
39 to integrate out the internal degrees of freedom, whereby an areal free-energy density can be defined.
40 The procedure is similar in spirit to the construction of interatomic potentials, for which the (quantum-
41 mechanical ground-state) fluctuations of electrons are integrated out rather than the (thermal) fluctuations
42 of internal elastic degrees of freedom.

43 In our first attempt on constructing effective surface interactions, we restrict our attention to the oldest,
44 and arguably most commonly used model for the interactions between surfaces, namely a non-overlap
45 constraint. Depending on context and dimension, it can also be called hard-wall, hard-disk, or hard-sphere
46 repulsion, which, by definition is infinitesimally short ranged. Since atoms fluctuate about their equilibrium
47 sites in solids, thermal fluctuations automatically make repulsion effectively adopt a finite range.

48 The central goal of this study is to quantify the just-described effects and to ascertain if constitutive laws
49 obtained for flat walls can be applied to other systems, in particular to a Hertzian contact. A secondary goal
50 is to identify an analytical expression for the thermal corrections to the load-displacement relation in a
51 Hertzian contact.

2 MODEL AND NUMERICAL METHOD

52 2.1 Definition of the model and nomenclature

53 The model consists of a homogeneous, semi-infinite, elastic solid with an originally flat bottom surface,
54 which is pressed down against a continuous, perfectly rigid substrate being fixed in space. The latter,
55 which will also be called indenter, is either perfectly flat, i.e., $h(\mathbf{r}) = 0$, or parabola, in which case
56 $h(\mathbf{r}) = -r^2/(2R_c)$, where R_c is the radius of curvature. In order to reduce finite-size effects and to
57 simplify both analytical and numerical treatments, periodic boundary conditions are assumed by default
58 within the quadratic, interfacial plane.

59 The elastic surface is subjected not only to an external load per particle, l , squeezing it down against the
60 indenter but also to thermal fluctuations, as they would occur in thermal equilibrium at a finite temperature
61 T . We restrict our attention to frictionless contacts and small counterface slopes. This allows us to consider
62 only displacements of the elastic surface normal to the interface. As such, the elastic energy of the surface
63 can be written as a functional of the field $u(\mathbf{r})$ according to

$$U_{\text{ela}}[u(\mathbf{r})] = \frac{E^*A}{4} \sum_{\mathbf{q}} q |\tilde{u}(\mathbf{q})|^2. \quad (1)$$

64 Here, $u(\mathbf{r})$ states the z -coordinate of the elastic solid's bottom surface as a function of the in-plane
65 coordinate $\mathbf{r} = (x, y)$. E^* is the contact modulus, A the (projected) interfacial area, \mathbf{q} an in-plane wave

66 vector, and q its magnitude.

$$\tilde{u}(\mathbf{q}) = \frac{1}{A} \int d^2r e^{-i\mathbf{q}\cdot\mathbf{r}} u(\mathbf{r}) \quad (2)$$

67 denotes the Fourier transform of $u(\mathbf{r})$. The short-hand notation $u_0 = \tilde{u}(\mathbf{q} = 0)$ will be used for the
68 center-of-mass coordinate.

69 For flat indenters, only u_0 will be used to denote the mean distance, or gap, between indenter and the
70 solid surface. Here, we define the displacement d as a function of temperature and load according to

$$d(T, L) \equiv h_{\text{ind}}(r = 0) - \langle u(T, L, r \rightarrow \infty) \rangle, \quad (3)$$

71 where $\langle u(T, L, r \rightarrow \infty) \rangle$ is the thermal expectation value that the field $u(\mathbf{r})$ would have (infinitely) far
72 away from the top if the simulation cell were infinitely large. d is sometimes also called interference, as it
73 states an effective penetration of the indenter into the elastic solid.

74 It is discussed in the literature [17] how to extrapolate accurately $u(L, r)$ to $r \rightarrow \infty$ for all those cases, in
75 which an indenter acts relatively localized in the center of a finite simulation cell. However, in the current
76 work, we are interested mostly in the temperature-induced reductions of d , i.e., in the term d_T defined in
77 the expression

$$d = d_0 - d_T, \quad (4)$$

78 where d_0 denotes the displacement for an ideal, athermal Hertzian indenter at a given load. In the current
79 work, we compute d_T through the following approximation

$$d_T \approx \langle u(T, L, \mathbf{r}_X) \rangle - u(0, L, \mathbf{r}_X), \quad (5)$$

80 where \mathbf{r}_X is the point that is the most distant from the center of the Hertzian indenter. We found that the
81 first three to four digits are accurate in this estimate if the athermal Hertzian contact radius is less than
82 one quarter of the simulation cell's linear dimension. This is because the (true) surface displacement fields
83 converge quite quickly to their asymptotic $1/r$ form outside the (original) contact radius in the case of
84 short-ranged potentials and because the finite-size corrections to the true surface displacements are not
85 very sensitive to temperature.

86 The interaction with a counterface is modeled within the Derjaguin approximation [18] so that the surface
87 energy density depends only on the local interfacial separation, or, gap, $g(\mathbf{r}) = u(\mathbf{r}) - h(\mathbf{r})$, between the
88 surfaces, i.e., the interaction potential is obtained via an integration over the surface energy density $\gamma(g)$ via

$$U_{\text{int}} = \int_A d^2r \gamma\{g(\mathbf{r})\}, \quad (6)$$

89 In the full microscopic treatment, hard-wall repulsion is assumed, i.e.,

$$\gamma(g) = \begin{cases} \infty & \text{if } g < 0 \\ 0 & \text{else.} \end{cases} \quad (7)$$

90 Finally, the probability of a certain configuration to occur is taken to be proportional to the Boltzmann
91 factor, i.e.,

$$\text{Pr}[u(\mathbf{r})] \propto e^{-\beta(U_{\text{ela}} + U_{\text{int}})}, \quad (8)$$

92 where $\beta = 1/k_B T$ is the inverse thermal energy.

93 One central “observable” in this work is the distance dependence of the mean force per atom, $f(u_0)$, for
 94 flat surfaces and finite temperatures. One might want to interpret this function as a cohesive-zone model, or,
 95 in the given context better as a repulsive-zone model. Because of the so-called equivalence of ensembles,
 96 which is valid for sufficiently large, systems, it does not matter if the separation is fixed and the force
 97 measured, or, vice versa.

98 Note that we will go back and forth between continuous and discrete descriptions of displacement fields.
 99 For the discrete description, the elastic solid is partitioned into atoms, which are arranged on a square
 100 lattice with the lattice constant Δa . This was done for reasons of simplicity, even if other discretizations
 101 are possible, e.g., into a triangular lattice [15]. Transitions between discrete and continuous representations
 102 in real space can be achieved with the substitutions

$$\sum_n \dots \leftrightarrow \frac{1}{\Delta a^2} \int_A d^2 r \dots, \quad (9)$$

103 while transitions between summations and integrals in the wavevector domain can be achieved with

$$\sum_{\mathbf{q}} \dots \leftrightarrow \frac{A}{(2\pi)^2} \int d^2 q \dots. \quad (10)$$

104 To simplify the analytical evaluation of integrals, the square Brillouin zone (BZ) of the surface will be
 105 approximated with a circular domain. In this case, the upper cutoff for q is chosen to be $q_{\max} = \sqrt{4\pi}/\Delta a$
 106 as to conserve the number of degrees of freedom with respect to the original BZ.

107 2.2 Thermal GFMD

108 GFMD is a method allowing a linearly elastic boundary-value problem to be solved efficiently [15, 16].
 109 The (discretized) surface displacement field reflects the dynamical degrees of freedom. Elastic interactions
 110 are described in terms of appropriate elastic Green’s functions, which — in the case of in-plane spatial
 111 homogeneity and infinitely large (or periodically repeated) systems — are (block) diagonal in the Fourier
 112 representation. The simplest case, which is considered here, is a frictionless contact and a semi-infinite
 113 elastic substrate. The equations to be solved in GFMD — using the regular tricks of the trade — are

$$m_q \ddot{\tilde{u}}(\mathbf{q}) + \eta_q \dot{\tilde{u}}(\mathbf{q}) + \frac{q E^*}{2} \tilde{u}(\mathbf{q}) = \tilde{F}(\mathbf{q}, t), \quad (11)$$

114 where $\tilde{F}(\mathbf{q}, t)$ is the Fourier transform of all external forces acting on the surface atoms. The terms m_q and
 115 η_q represent inertia and damping coefficients of different surface modes, which may depend on the wave
 116 vector. For isotropic systems, these terms only depend on q but not on the direction of \mathbf{q} .

117 The effect of thermal fluctuations can be cast as random forces, which have to satisfy the fluctuation-
 118 dissipation theorem (FDT) [19]. In the given formalism, random forces must have a zero mean, while their
 119 second moments must satisfy,

$$\langle \Gamma(\mathbf{q}, t) \Gamma(\mathbf{q}', t') \rangle = 2 \eta_{\mathbf{q}} k_B T \delta_{\mathbf{q}, \mathbf{q}'} \delta(t - t'), \quad (12)$$

120 assuming discrete atoms, finite domains but continuous times. Here, $\delta(\dots)$ is the Dirac delta function, which
 121 can be replaced with $\delta_{t,t'}/\Delta t$ in a molecular dynamics (MD) simulation, in which the time t is discretized
 122 into steps of size Δt .

123 At this point, GFMD is only used to generate the correct distribution of configurations, which—in a
 124 classical system—does not depend on the choice of inertia. As such, the m_q can be chosen at will as far
 125 as static observables are targeted. However, in order to reproduce realistic dynamics, appropriate choices
 126 for m_q and η_q have to be made. In fact, realistic dynamics require the treatment of damping and random
 127 noise to have “memory”, as discussed in Ref. [20]. When being interested in fast equilibration, the m_q
 128 are better chosen such that the usually slowly equilibrating long-wavelength modes are made light so that
 129 characteristic times for different modes coincide as closely as possible [16]. In this context, it is also worth
 130 mentioning that significant progress has been made recently on GFMD to properly reflect not only true
 131 (rather than efficient) dynamics of crystalline solids [21] but also for truly visco-elastic materials with
 132 broad relaxation functions [22].

133 2.3 Hard-wall interactions in thermal GFMD

134 Non-overlap constraints can be implemented in athermal GFMD by placing any atom, predicted to have
 135 penetrated the rigid solid, back onto its surface. This procedure no longer works at finite temperatures. It
 136 violates the FDT because the damping that is effectively imposed by this algorithm, is not compensated by
 137 a conjugate random force.

138 The standard way of treating hard-wall or hard-disk interactions is to make it make the time step so large
 139 that the next collision between two hard sphere occurs at the end of it. Before proceeding with the time
 140 stepping, an ideal, elastic collision is then assumed. This course of action does not appear to be viable for
 141 contact mechanics, because it would lead to prohibitively small time steps for large-scale contacts, where
 142 several (hundred) thousands of grid points are usually classified as being in contact. Specifically, when
 143 doubling the system size N , the typically allowed time step will have to be halved on average so that the
 144 asymptotic computational effort would scale with N^2 rather than with N or $N \ln N$.

145 2.3.1 Effective hard-wall potentials

146 An alternative to the standard ways of implementing non-overlap constraints is to allow its violation in a
 147 controlled fashion. For example, the true hard-wall interaction can be replaced with a finite-range energy
 148 density penalty of the form

$$\gamma(g) = \frac{\kappa_o E^* \Delta a}{n} \left(\frac{-g}{\Delta a} \right)^n \Theta(-g) \quad (13)$$

149 where Θ is the Heavyside step function and κ_o and n are dimensionless parameters. In loose analogy
 150 to a Richardson extrapolation, an observable of interest O can be computed for a fixed exponent n but
 151 different values of κ_o . Finally, the results can be extrapolated to hard-wall interactions by investigating the
 152 asymptotics of $O(1/\kappa)$ in the limit of $1/\kappa \rightarrow 0$. Large values of κ_o will limit the time step Δt . However,
 153 these limits do not depend on system size. Thus, the numerical effort will scale with $O(1/N)$ rather than
 154 with $O(1/N^2)$ as is the case when dynamics are based on the more accurate, flexible time-step collision
 155 dynamics.

156 Good numbers for the exponent n and the dimensionless hard-wall stiffness κ_o need to be chosen. In
 157 order for the effective hard-wall potential to have a minimal effect on Δt , the (non-negative) exponent n
 158 should be as small as possible. However, we would like the force to be a continuous function, for reasons
 159 explained at length in any better text book on molecular dynamics [11, 12]. While these arguments can be

160 somewhat academic when the discontinuities are small, we are going to send κ_o to large numbers resulting
 161 in significant force discontinuities. Thus, n must be chosen greater equal two. This appears to make $n = 2$
 162 the optimal choice.

163 The next question to be answered is: Given a time step Δt and an exponent of $n = 2$, what is a good value
 164 for κ_o ? Here, it is useful to keep in mind that we do not need very accurate dynamics in the “forbidden”
 165 overlap zone. The main purpose of the stiff harmonic potential is to eliminate overlap as quickly as possible,
 166 i.e., to effectively realize a collision of the particles with the position of the (original) hard wall. However,
 167 the stiffness should remain (well) below a critical value above which energy conservation is violated in
 168 the absence of a thermostat even when a symplectic integrator, such as the Verlet algorithm, is used. For
 169 Verlet, the critical time step for a harmonic oscillator is $\Delta t_c = T/\pi$, where T is the oscillator period, i.e.,
 170 for $\Delta t < \Delta t_c$, the trajectory may be inaccurate, but the energy is conserved (except for round-off errors).
 171 This can be achieved by setting the overlap stiffness to

$$k_o = \nu_o \pi^2 \frac{m}{dt^2} - k_s, \quad (14)$$

172 where $k_s = \Delta u^2/(k_B T)$, while m is the inertia of the considered degree of freedom. ν_o is a numerical
 173 factor, which must be chosen less than unity. At and above the critical value of $\nu_o = 1$, energy conservation
 174 would be no longer obeyed in the absence of a thermostat. At the same time, dynamics but also static
 175 distribution functions are very inaccurate, even if a thermostat prevents the system from blowing up.

176 The optimum value for k_o certainly depends on the specific investigated problem. However, the analysis
 177 of simple models can provide useful preliminary estimates. This will be done in Sect. 2.3.3.

178 2.3.2 Approximate collision rules

179 A second possibility to avoid the poor efficiency of exact collision dynamics is to use approximate
 180 collision rules and to control the error of the imprecision with the time step. A simple possibility would be
 181 to keep Δt fixed in a simulation and to make the deflection of the atom after the regular time stepping. For
 182 example, when using velocity Verlet, the following pseudo code could be invoked after a regular time step,
 183 in which the constraint was ignored:

```
184 if (z violates constraint) then
185     z = 2zconstr - z
186     vz = -vz           (velocity Verlet)
187     zold = 2zconstr - zold (standard Verlet)
188 end if
```

189 Note that this approach requires extra care to be taken when dynamics are formulated in a wavevector
 190 representation, which is usually the case in efficient boundary-element methods. If implemented the
 191 following overhead would have to be realized: old positions (or velocities) in real space will then have to
 192 be kept in memory. Moreover, two additional Fourier transforms will have to be invoked in each time step,
 193 which would double the number of the (asymptotically) most expensive function calls. Since approximate
 194 collision dynamics turn out to show similar scaling with Δt in simple models as effective hard-wall
 195 repulsion, see Sect. 2.3.3, we did not pursue approximate collision rules further at this point of time in the
 196 full contact-mechanics simulations.

197 2.3.3 Numerical case studies

198 To explore the relative merit of the two proposed hard-wall methods, we investigate the following
 199 single-particle problem: an originally free, harmonic oscillator with a (thermal) variance of Δu^2 . This
 200 harmonic oscillator is then constrained to have no negative deflections from its mechanical equilibrium
 201 site. The analytical solution to this problem stating the force F needed to realize a given constraint is
 202 contained in the mean-field approximation to the full elastic problem, which is presented in Sect. 3.2.2.
 203 The given constraint of the spring sitting exactly on the hard wall corresponds to a value, where $\langle u_0 \rangle$
 204 crosses over from its short-range to its long-range asymptotic behavior. Therefore, we see this case as
 205 being representative for both scaling regimes.

206 In essence, the problem we investigate corresponds to the choice where $k_B T$, k , and m are used to define
 207 the unit system, which makes Δu^2 being unity (in units of $k_B T/k$) as well. The default time step that we
 208 use for the free oscillator is $2\pi/30$, i.e., 30 time steps per period. The damping coefficient is chosen to be
 209 $\gamma = 1$, whereby the free harmonic oscillator is slightly underdamped. While this choice is not necessarily
 210 ideal, it still tends to be effective for a fast equilibration, irrespective of whether the temperature is zero or
 211 finite. Results for the convergence of how the estimate for the mean displacement u_0 approaches the exact
 value with decreasing time step Δt are shown in Fig. 1

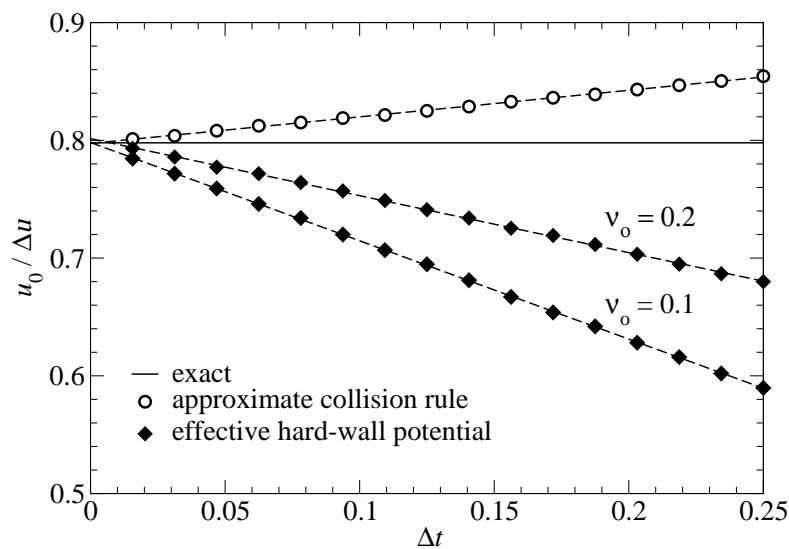


Figure 1. Mean displacement u_0 as a function of time step Δt when using (a) approximate collision rules (open circles) and (b) harmonic effective hard-wall potentials (closed diamonds) for two different values of ν_o , see Eq. (14). Dashed lines show linear fits, the solid line the exact, analytical solution. The equilibrium site of the spring is placed at $u_s = 0$, moreover $\Delta u^2 = k_B T = 1$.

212

213 At a given value of Δt , the approximate collision rules clearly outperform the approximate hard-wall
 214 interactions. However, u_0 has leading-order corrections of order Δt in both approaches. With the choice
 215 $\nu_o = 0.1$, the asymptotic result for the parabolic, effective hard-wall potential has an accuracy of better
 216 than 1%, which should be accurate enough for most purposes. In both approaches, simulations must be

217 run at two different values of Δt , say e.g., at $\Delta t = 0.25$ and $\Delta t = 0.15$ in order to perform a meaningful
 218 $\Delta t \rightarrow 0$ extrapolation. In a full contact-mechanics simulation, the number of required Fourier transforms
 219 doubles when using the approximate collision rules, which in turn leads to increased stochastic errors given
 220 a fixed computing time contingent. For this reason, but also because approximate collision rules require
 221 significantly more coding—in particular when averaging wall-surface forces from collisions when using
 222 wavevector dependent inertia—we decided to use the harmonic, effective hard-wall potential for the full
 223 contact-mechanics simulations.

3 THEORY

224 The main purpose of this section is to identify an analytical expression for the thermal expectation value
 225 of an interfacial force per atom $f(u_0)$ as a function of their mean separation u_0 in the case of a hard wall.
 226 This will be done by defining the partition function $Z(N, \beta, u_0)$ of a fluctuating surface in front of a wall,
 227 which is linked to the free energy through the relation $\mathcal{F}(k_B T, u_0) = -k_B T \ln Z(\beta, u_0)$. The mean force
 228 between hard wall and elastic surface can then be calculating from

$$f = -\frac{1}{N} \frac{\partial \mathcal{F}(N, k_B T, u_0)}{\partial u_0}. \quad (15)$$

229 Minor errors in the treatment presented below appear in numerical coefficients that result, for example,
 230 by having approximated the Brillouin zone of a square with a sphere, or, by having replaced a discrete set
 231 of wave vectors (finite system) with a continuous set (infinitely large system). However, these and related
 232 approximations are controlled, because errors resulting from them can be estimated and they could even be
 233 corrected systematically.

3.1 The statistical mechanics of a free surface

235 Since the free surface is the reference state, we start with its discussion. An important quantity, in
 236 particular in a mean-field approach, is the variance of atomic displacements due to thermal noise. For a
 237 fixed center-of-mass coordinate, it is defined as the following thermal expectation value:

$$\Delta u^2 \equiv \langle \{u(\mathbf{r}) - \tilde{u}(0)\}^2 \rangle. \quad (16)$$

238 It can be evaluated in its wavevector representation in a straightforward manner. Specifically,

$$\Delta u^2 = \sum_{\mathbf{q}'} \langle |\tilde{u}(\mathbf{q}')|^2 \rangle \quad (17)$$

$$\approx \frac{A}{(2\pi)^2} \int d^2 q \frac{2 k_B T}{q E^* A} \quad (18)$$

$$\approx \frac{2}{\sqrt{\pi}} \frac{k_B T}{E^* \Delta a}, \quad (19)$$

239 where we made use of equipartition for harmonic modes, see also Eq. (29).

240 Of course, up to the prefactor of $2/\sqrt{\pi} \approx 1.1284$, which is very close to unity, Eq. (19) follows directly
 241 from dimensional analysis. However, in a quantitative theory, we wish to know and perhaps to understand
 242 its precise value. A numerical summation over a square BZ assuming a square real-space domain with N

243 atoms reveals that Δu^2 can be described by

$$\Delta u^2 = \left(1.1222 - \frac{1.24}{\sqrt{N}}\right) \frac{k_B T}{E^* \Delta a}, \quad (20)$$

244 with more than three digits accuracy if $\sqrt{N} > 512$. This result is fairly close to the analytical result based
245 on a BZ, which is approximated as sphere.

246 Assuming discretization down to the atomic scale of $\Delta a \approx 2.5 \text{ \AA}$ yields a root-mean square (rms) height
247 of

$$\Delta u \approx 1.5 \sqrt{\text{GPa}/E^*} \text{ \AA} \quad (21)$$

248 at room temperature. Thus, for soft-matter systems, the effect of thermal fluctuations is not necessarily
249 non-negligible at room temperature. The dominant restoring forces to height fluctuation at short scales will
250 then be due to surface tension rather than due to elasticity [23]. However, it might be possible to suppress
251 those effects when immersing the surfaces into an appropriate liquid, e.g., crosslinked polyethylene glycol
252 (PEG) into uncrosslinked PEG.

253 An outcome of Eq. (19) is that the fluctuations are dominated by the small scales. In the simplest
254 approximation, which can be made in direct association with the Einstein model of solids, each surface
255 atom is coupled harmonically to its lattice site with a spring of stiffness $k_E = k_B T / \{(N - 1) \Delta u^2\}$. In
256 reality, i.e., in less than infinite dimensions, there is always a correlation of thermal height fluctuations.

257 To deduce an estimate for the distance over which height fluctuations are correlated, we calculate the
258 thermal displacement autocorrelation function (ACF) $C_{uu}(r)$. It can be defined and evaluated to obey:

$$C_{uu}(\Delta r) = \langle u(\mathbf{r}) u(\mathbf{r} + \Delta \mathbf{r}) \rangle \quad (22)$$

$$\approx \frac{1}{2\pi^2} \frac{k_B T}{q E^*} \int_0^{\sqrt{4\pi}/\Delta a} dq \int_0^{2\pi} d\varphi e^{iqr \cos \varphi} \quad (23)$$

$$= \frac{1}{\pi} \frac{k_B T}{r q E^*} \int_0^{\sqrt{4\pi} r / \Delta a} d(qr) J_0(qr) \quad (24)$$

$$= \frac{2 k_B T}{q E^*} \frac{\sqrt{4\pi} r}{\Delta a} {}_1F_2 \left(\frac{1}{2}; 1, \frac{3}{2}; \frac{-\pi r^2}{\Delta a^2} \right) \quad (25)$$

$$\approx \begin{cases} \frac{2 k_B T}{\sqrt{\pi} E^* \Delta a} + \mathcal{O}(r^2) & \text{for } r \rightarrow 0 \\ k_B T / (\pi q E^* r) & \text{for } r \rightarrow \infty, \end{cases} \quad (26)$$

259 where $J_0(x)$ is the Bessel function of the first kind and ${}_1F_2(\dots)$ is a generalized hypergeometric function.
260 Unfortunately, the result obtained analytically this way shows Helmholtz ringing at intermediate values
261 of r (i.e. within a substantial range of Δu), which is why the exact analytical solution for $C_{uu}(r)$ is of
262 little practical use, except in the two limiting cases $r = 0$ and $r \rightarrow \infty$. Helmholtz ringing is generally a
263 consequence of sharp cutoffs in the wave vector domain. Interestingly, it persists even for a square BZ
264 when the exact expectation values for $|\tilde{u}(\mathbf{q})|^2$ are used and the correlation function $C_{uu}(\mathbf{r})$ is extended to
265 the continuous domain between the lattice positions. The validity of these claims is demonstrated in Fig. 2.

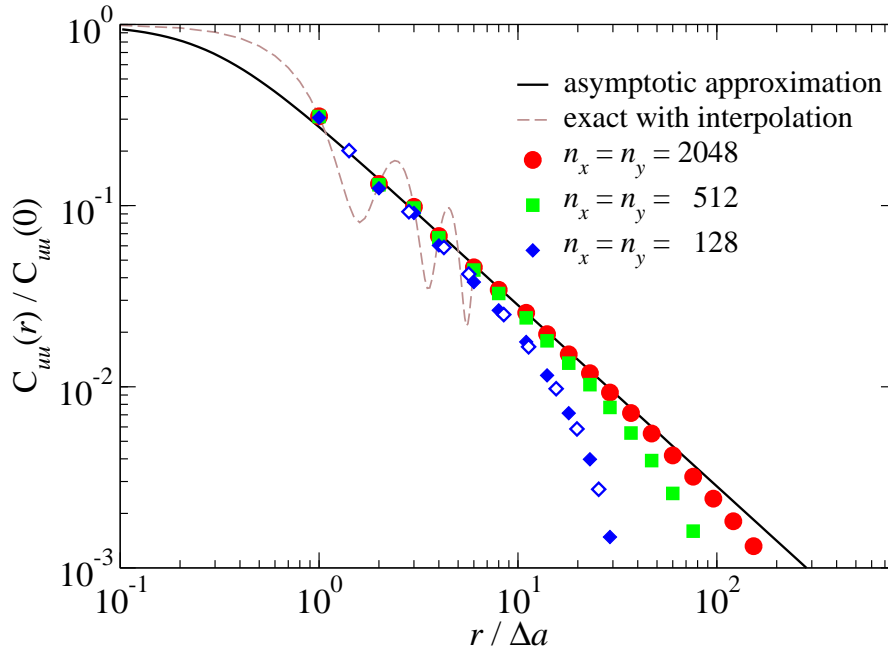


Figure 2. The radial displacement ACF $C_{uu}(r)$ —normalized to its value at $r = 0$ —as a function of distance r : asymptotic approximation given in Eq. (27) (black line), exact correlation function along the [10] direction with interpolation between non-lattice sites (dashed brown line), numerically exact results for systems of size 2048×2048 (red circles), 512×512 (green squares), and 128×128 (blue diamonds). They were also obtained for the [10] direction, except for the open symbols, which refer to the [11] direction.

266 A quite reasonable approximation or rather generalization of $C_{uu}(r)$ to a continuous function can be made
 267 by constructing the simplest expression with the correct asymptotic behaviors summarized in Eq. (26):

$$C_{uu}(r) \approx \frac{2}{\sqrt{\pi}} \frac{k_B T}{E^*} \frac{1}{(\Delta a^2 + 4\pi r^2)^{1/2}}. \quad (27)$$

268 As can be seen in Fig. 2, this asymptotic approximation is quite reasonable already at a nearest-neighbor
 269 spacing of $r = \Delta a$ and has errors of less than 5% (in the limit of large N) for larger values of r . While
 270 numerical results for finite systems in Fig. 2 include predominantly data for \mathbf{r} parallel to $[1, 0]$, similar
 271 results are obtained for other directions as well, as demonstrated exemplarily for the $[1, 1]$ direction of the
 272 $N = 128 \times 128$ lattice.

273 The asymptotic ACF has decayed to approximately 30% of its maximum value at the nearest-neighbor
 274 distance. This means that the displacements of adjacent lattice sites are essentially uncorrelated.

275 The last property of interest used in the subsequent treatment is the partition function of a free surface
 276 (fs):

$$Z_{\text{fs}}(\beta) = \prod_{\mathbf{q}} \frac{\lambda_{\mathbf{q}}}{\sqrt{2\pi \Delta u^2(\mathbf{q})}} \quad (28)$$

277 with

$$\Delta u^2(q) = \frac{2 k_B T}{q E^* A}. \quad (29)$$

278 $\lambda_q = h/\sqrt{2 m_q k_B T}$ represents the thermal de Broglie wavelength of a surface mode. It reflects the
 279 ideal-gas contribution of the momenta conjugate to the $\tilde{u}(\mathbf{q})$ to the partition function. As long as E^* is
 280 small compared to the ambient pressure and as long as temperature is kept constant, the sole purpose of
 281 including λ_q into the calculation is to render the partition function dimensionless. This is why a precise
 282 determination of m_q , which might be an interesting topic in itself, is not needed at this point. If we had
 283 to determine the most meaningful value of m_q , our line of attack would be to calculate the quantum-
 284 mechanical zero-point vibrations of surface modes in a full description of the solid of interest (e.g., by
 285 using path-integral techniques [24]) and to assign m_q such that it reproduces the correct zero-point variance
 286 of the mode in question.

287 In the mean-field (Einstein solid) approximation, the partition function simplifies to

$$Z_{\text{mf}}(\beta) = \left(\frac{\lambda_{\text{mf}}}{\sqrt{2\pi\Delta u^2}} \right)^N, \quad (30)$$

288 with Δu having been introduced in Eq. (19) and λ_{mf} being a mean-field de Broglie wavelength.

289 3.2 Interaction of a thermal, elastic surface with a flat wall

290 In this section, we investigate the statistical mechanics of an elastic surface in front of a flat, hard wall. To
 291 this end we derive expressions for the partition function of the system, from which the mean force between
 292 surface and wall (at fixed mean separation) can be derived in a straightforward fashion. Different mean-field
 293 strategies will be pursued towards this end. They turn out to be quite accurate in different asymptotic limits
 294 of the full problem.

295 3.2.1 First mean-field approximation

296 The arguably simplest analytical approach to the contact problem is an adaptation of the so-called Einstein
 297 solid, which was already alluded to in Sect. 3.1, to surface atoms. We first do it such that a degree of
 298 freedom is a hybrid of an atom in real space and a delocalized, ideal sine wave. Specifically, we first assume
 299 that elastic energy of an individual atom reads

$$v_{\text{ela}}^{\text{mf}}(u) = \frac{k_B T}{2 \Delta u^2} u^2. \quad (31)$$

300 In order to maintain a zero expectation value of u , it is furthermore assumed that the interaction energy
 301 with a counterface placed at a distance u_0 from the atom's mean position is given by

$$v_{\text{sub}}^{\text{mf}}(u) = \frac{\Delta a^2}{2\pi} \int_0^{2\pi} d\varphi \gamma(u_0 + u \cos \varphi). \quad (32)$$

302 This means, an oscillation of an atom entails an undulation. With this assumption, u_0 automatically
 303 corresponds to the atom's mean position.

304 The excess free energy per particle $\Delta \mathcal{F}/N$ for a fixed center-of-mass position satisfies

$$e^{-\beta \mathcal{F}/N} = \frac{1}{\sqrt{2\pi\Delta u^2}} \int_{-\infty}^{\infty} du e^{-\beta \{v_{\text{ela}}^{\text{mf}}(u) + v_{\text{sub}}^{\text{mf}}(u)\}}, \quad (33)$$

305 where the term “excess” refers to the change of the free energy relative to that of a free surface. For
 306 hard-wall interactions, the integral in Eq. (33) can be evaluated to be

$$\begin{aligned} e^{-\beta\mathcal{F}/N} &= \frac{1}{\sqrt{2\pi\Delta u^2}} \int_{-u_0}^{u_0} du e^{-\beta v_{\text{ela}}(u)} \\ &= \text{erf}\left(\frac{u_0}{\sqrt{2}\Delta u}\right). \end{aligned} \quad (34)$$

307 Hence,

$$\frac{\mathcal{F}}{N k_B T} = -\ln\left\{\text{erf}\left(\frac{u_0}{\sqrt{2}\Delta u}\right)\right\} \quad (35)$$

$$\approx \begin{cases} -\ln\left(\sqrt{\frac{2}{\pi}} \frac{u_0}{\Delta u}\right) & \text{for } u_0 < \Delta u/2 \\ \frac{\Delta u}{\sqrt{\pi}u_0} e^{-u_0^2/(2\Delta u^2)} & \text{for } u_0 > 2\Delta u. \end{cases} \quad (36)$$

308 For reasons of completeness, the force predicted from this first mean-field approximation is stated as:

$$f_{\text{mf1}}(u_0) = \sqrt{\frac{2}{\pi}} \frac{k_B T}{\Delta u} \frac{\exp\{-u_0^2/(2\Delta u^2)\}}{\text{erf}\{u_0/(\sqrt{2}\Delta u)\}}. \quad (37)$$

309 In the limit of $u_0 \rightarrow 0$, repulsion diverges proportionally with $1/u_0$, while it decays slightly quicker than
 310 exponentially in u_0^2 for separations $u_0 \gg \Delta u$. Both limiting behaviors are confirmed in the results section,
 311 albeit, with a prefactor of a little less than one half for large separations.

312 3.2.2 Second mean-field approximation

313 Another mean-field approach would be to abandon the evaluation of the interaction in terms of an
 314 undulation and to introduce a Lagrange parameter, i.e., an external force f divided by the thermal energy,
 315 ensuring u to adopt the desired value of u_0 . Thus, the probability of a displacement u to occur satisfies

$$\text{Pr}(u) \propto e^{-(u-u_0)^2/(2\Delta u^2) - \beta f(u-u_0)} \Theta(u), \quad (38)$$

316 where f needs to be chosen such that $\langle u \rangle = u_0$ so that the lattice position of the particle u_{eq} is situated
 317 at $u_{\text{eq}} = u_0 + \beta f \Delta u^2$. At u_{eq} , there is no elastic restoring force in the spring. The requirement $\langle u \rangle = u_0$
 318 automatically leads to the following self-consistent equation for f :

$$\beta f \Delta u = \sqrt{\frac{2}{\pi}} \frac{\exp\left\{-\frac{(\beta f \Delta u^2 - u_0)^2}{2\Delta u^2}\right\}}{1 - \text{erf}\left(\frac{\beta f \Delta u^2 - u_0}{\sqrt{2}\Delta u}\right)}. \quad (39)$$

319 This line of attack leads to similar results for the $f(u_0)$ at small u_0 as the first mean-field approach.
 320 However, for large u_0 the predicted force turns out half that of the first mean-field approximation. In fact,
 321 the second mean-field theory turns out to be a quite reasonable approximation to the numerical data for any
 322 value of Δu , see the results and discussion presented in Sect. 4.

323 3.2.3 Probabilistic approach

324 The exact expression for the excess free energy of an elastic body in front of a hard wall can be defined
325 by a path integral,

$$e^{-\beta\mathcal{F}(u'_0)} = \frac{1}{Z_A} \int \mathcal{D}[u(\mathbf{r})] \delta(u'_0 - u_0) e^{-\beta v_{\text{tot}}[u(\mathbf{r})]}, \quad (40)$$

326 where $\mathcal{D}[u(\mathbf{r})]$ denotes an integral over all possible displacement realizations and

$$Z_A = \int \mathcal{D}[u(\mathbf{r})] \delta(u_0 - u'_0) e^{-\beta v_{\text{ela}}[u(\mathbf{r})]}. \quad (41)$$

327 In the case of hard-wall repulsion, the r.h.s. of Eq. (40) is easy to interpret: It represents the relative number
328 of configurations that are produced with the thermal equilibrium distribution of a free surface (fs), whose
329 maximum displacement is less than u_0 , i.e.,

$$e^{-\beta\mathcal{F}(u_0)} = \langle \text{Pr}(u_{\text{max}} < u_0) \rangle_{\text{fs}}, \quad (42)$$

330 This insight defers the problem of having to solve the path-integral in Eq. (40) to an exercise in probability
331 theory: determine the likelihood of $N' = N\Delta a^2/\Delta A_c$ independent Gaussian random number with mean
332 zero and variance Δu^2 to be less than u_0 . Here ΔA_c is the correlation area for the displacements. Given
333 that $C_{uu}(\Delta r)$ has decayed to a few 10% at nearest-neighbor distances, it can only be marginally larger
334 than Δa^2 .

335 For large values of N' , the distribution of maximum values $u_{\text{max}} = \max\{u(\mathbf{r})\}$ converges to the Gumbel
336 distribution, also known as the generalized extreme value (gev) distribution type-I [25]. It is given by

$$\text{Pr}(u_{\text{max}}) = \frac{1}{\beta_{\text{gev}}} e^{-(e^{-z})} \quad (43)$$

337 with

$$z = \frac{u_{\text{max}} - \mu_{\text{gev}}}{\beta_{\text{gev}}}, \quad (44)$$

338 where μ_{gev} is the mode of the Gumbel distribution, i.e., the most likely value for u_{max} to occur, and β_{gev} a
339 parameter determining the shape of the distribution. For a normal Gaussian distribution $\Phi_G(u/\Delta u)$, they
340 are given by

$$\frac{\mu_{\text{gev}}}{\Delta u} = \sqrt{2} \text{erf}^{-1} \left(1 - \frac{2}{N'} \right) \quad (45)$$

$$\frac{\beta_{\text{gev}}}{\Delta u} = \frac{1}{N' \cdot \Phi_G(\mu_{\text{gev}}/\Delta u)} \quad (46)$$

341 in the limit of large N' . Here $\text{erf}^{-1}(\dots)$ stands for the inverse function of the error function [25].

342 In fact, Fig. 3 shows that the distribution of u_{max} as produced with GFMD and by taking the maximum
343 value of $N' = 0.92N$ independent random numbers are essentially identical and that both can be
344 approximated quite well with the Gumbel distribution. If setting $N' = N$, the (open) symbols in Fig. 3
345 would shift by roughly half their symbol size to the right. As expected, discrepancies between the Gumbel
346 distribution and the numerical data decrease with increasing N' .

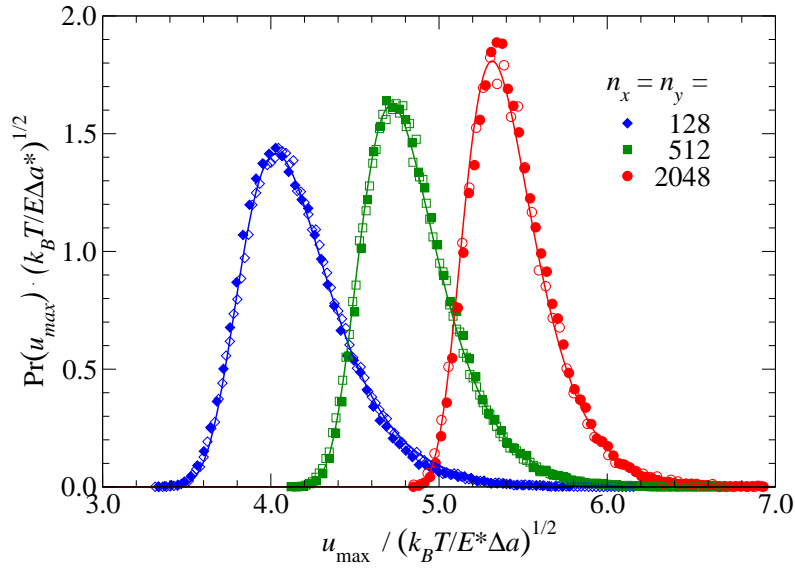


Figure 3. Distribution of maximum displacements for different system sizes as obtained from GFMD (closed symbols). Considered system sizes are $N = 128 \times 128$ (diamonds), 512×512 (squares), 2048×2048 (circles). Comparison is made to the distribution of the maximum of $N' = 0.92 N$ independent random numbers of mean zero and variance Δu (open symbols) as well as to the corresponding Gumbel distribution.

347 Rather than relying on the Gumbel distribution, one might as well write down the exact probability of one
 348 positive Gaussian random variable (grv) to be less than u_0 and take the result into the $N'/2$ -th power. (On
 349 average, there are $N'/2$ positive grv's, whose value may not exceed u_0 . The negative grv's are irrelevant
 350 with respect to the violation of the violation of the non-overlap constraint.) In this approximation,

$$\Pr(u_{\max} < u_0) = \left\{ \operatorname{erf} \left(\frac{u_0}{\sqrt{2}\sigma} \right) \right\}^{N'/2}. \quad (47)$$

351 and therefore

$$\Delta \mathcal{F} = -\frac{N' k_B T}{2} \ln \left\{ \operatorname{erf} \left(\frac{u_0}{\sqrt{2}\Delta u} \right) \right\}. \quad (48)$$

352 This result turns out to apply to large separations, that is, to $u_0/\Delta u \gg 1$. The functional form of $\mathcal{F}(u)$ is
 353 identical to the one obtained in the first mean-field variant, except for the prefactor, which is reduced by a
 354 little more than a factor of two.

355 3.3 Thermal Hertzian contacts

356 3.3.1 Preliminary considerations

357 At small temperatures, the relative leading-order corrections to the zero-temperature displacement
 358 $u_0(T = 0)$ can be expected to depend on powers of the variables defining the problem, i.e.,

$$\frac{d_T}{d_0} \propto \left(\frac{R_c}{\Delta a} \right)^\alpha \left(\frac{E^* R_c^2}{L} \right)^\beta \left(\frac{k_B T}{E^* R_c^3} \right)^\gamma, \quad (49)$$

359 where the contact modulus E^* and the contact radius R_c were effectively used to define the units of pressure
 360 and length, respectively. With the help of a further dimensional analysis, which can be conducted in a
 361 similar fashion as that in Ref. [17], the sum rule

$$\alpha + 3\beta - 5\gamma = 0 \quad (50)$$

362 follows immediately for the exponents introduced on the r.h.s. of Eq. (49). This relation is valid for
 363 a quadratic tip shape, linear elasticity, assuming the interfacial stress is a function of $u(r)/\Delta u$ with
 364 $\Delta u \propto \sqrt{T}$.

365 The r.h.s. of Eq. (49) and the sum rule for exponents in Eq. (50) can also be valid at high-temperatures.
 366 However, different exponents will apply. At intermediate temperatures, an expansion over terms such as
 367 those discussed so far are the only possibility to conform to the dimensional analysis.

368 3.3.2 Low-temperature approximation

369 At very small temperatures, the stress profile can be expected to differ only marginally from that of
 370 the athermal contact. In a perturbative approach to the problem, one could therefore assume that the
 371 most important correction to the original Hertzian gap $g_H(r)$ is a constant shift by d_T . The latter can be
 372 determined by minimizing the thermal excess energy per atom

$$e_T = -d_T L + \frac{1}{\Delta a^2} \int d^2r \mathcal{F}_{\text{pa}} \{g_H(r) + d_T\} \quad (51)$$

$$\approx -d_T L + \frac{2\pi}{\Delta a^2} \int_0^{a_c} dr r \mathcal{F}_{\text{pa}}(d_T), \quad (52)$$

373 where $\mathcal{F}_{\text{pa}} \equiv \mathcal{F}/N$ denotes the hard-wall, free-energy normalized to the atom. The approximation in
 374 Eq. (52) is motivated by the expectation that the dominant contribution to e_T resides within the original
 375 contact area. Minimization of e_T w.r.t. d_T leads to

$$L = \frac{\pi a_c^2}{\Delta a^2} f(d_T) \quad (53)$$

$$\approx \frac{\pi a_c^2}{\Delta a^2} \sqrt{\frac{2}{\pi}} \frac{k_B T}{\Delta u} \frac{\exp(-u_0^2/2\Delta u^2)}{\text{erf}(u_0/\sqrt{2}\Delta u)} \quad (54)$$

376 where the last approximation is only valid at small temperatures. Taylor expanding this last expression
 377 leads to

$$\frac{d_T}{d_0} \approx \frac{T}{T^*} \quad (55)$$

378 with

$$T^* = \frac{L \Delta a^2}{\pi k_B R_c}. \quad (56)$$

379 3.3.3 High-temperature approximation

380 At very large temperatures, d_T is in excess of d_0 so that deformations of the elastic solids are very small.
 381 In a first-order perturbative approach, it then makes sense to assume the displacement field to be a constant,
 382 i.e., to be d_T . In that approximation, individual forces can be simply summed up with a mean gap of

383 $d_T + r_n^2/(2R_c)$. Recasting the sum as an integral yields

$$L \approx \frac{N'}{2N} \frac{1}{\Delta a^2} \int d^2r f_{\text{mf1}} \left(d_T + \frac{r^2}{2R_c} \right) \quad (57)$$

$$\approx L_0 \frac{\Delta u}{d_T} e^{-d_T^2/(2\Delta u^2)} \quad (58)$$

384 with

$$L_0 = \sqrt{\frac{2}{\pi}} \frac{N'}{N} \frac{k_B T R_c}{\Delta a^2}. \quad (59)$$

385 Eq. (58) can be solved for d_T with the help of the Lambert W function $W(x) \approx \ln x - \ln \ln x$ for $x \gg 1$:

$$\frac{d_T}{\Delta u} \approx \sqrt{W \left(\frac{L_0^2}{L^2} \right)}. \quad (60)$$

4 RESULTS

386 4.1 Potential of mean force for a flat hard wall

387 In this section, we investigate to what extent the three approaches introduced in Sect. 3.1 reproduce
 388 accurate, numerical results for the thermal repulsive-zone model. To this end, we chose units such that
 389 $E^* = 1$ and $\Delta a = 1$ and consider different values of $u_0/\Delta u$, which is the only dimensionless variable for
 390 the given problem besides the system size, which is varied as well.

391 Fig. 4 compares GFMD data to the various approximative approaches introduced in Sect. 3. The first
 392 mean-field approach appears to be asymptotically exact for small u_0 , while the approach based on the law
 393 of large numbers seems to be asymptotically exact for large u_0 . In between these two regimes, there is a
 394 smooth transition between them. This transition is reflected quite well by the second mean-field approach.
 395 Unfortunately, we did not identify a closed-form analytical expression for it, which would nevertheless be
 396 nice to have when implementing a potential of mean force into a simulation. However, as is demonstrated
 397 in Fig. 4, simple switching functions introduced next allow one to approximate numerical data reasonably
 398 well.

399 Since both force-distance asymptotic dependencies have the same functional form and since the transition
 400 between them is quite continuous, it is relatively easy to come up with switching functions allowing
 401 the numerically determined free energy to be approximated reasonably well. Defining \mathcal{F}_{mf1} through the
 402 free-energy expression in Eq. (35), this is done via

$$\mathcal{F}(u_0) \approx w_1(u_0) \mathcal{F}_{\text{mf1}}(u_0) + w_2(u_0) \Delta \mathcal{F} \quad (61)$$

403 with the weighting functions

$$w_1(u_0) = \frac{1}{2} \left\{ \frac{N'}{N} + \left(2 - \frac{N'}{N} \right) e^{-u_0^2/\Delta u^2} \right\} \quad (62)$$

$$w_2(u_0) = e^{-u_0^2/\Delta u^2} \{ 1 - \tanh(u_0/\Delta u) \} \quad (63)$$

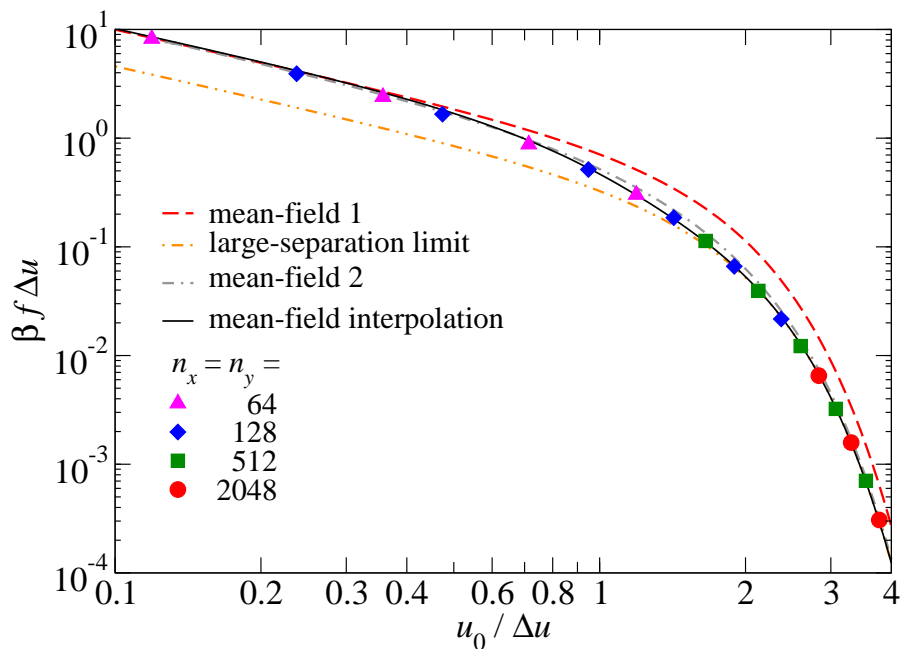


Figure 4. Mean force f , in units of $1/\beta\Delta u$, as a function of normalized mean separation $u_0/\Delta u$, where Δu represents the height standard deviation of a surface atom in the absence of a counterface.

404 The numerical value for $\Delta\mathcal{F}$ turned out to be $\Delta\mathcal{F} = -N'k_B T/2$. The forces $f(u)$ in a coarse-grained
 405 description are obtained as negative derivative by differentiating the r.h.s. of Eq. (61). The resulting
 406 expression corresponds to the numerical GFMD data for systems with $n_x = n_y \geq 128$ with maximum
 407 errors less than 10%, at least when taking the exact value for Δu^2 .

408 In terms of an efficient implementation of the method, we recommend to use tabulated expressions for
 409 $f(u)$ for intermediate values of u and the asymptotic expressions for $u \ll \Delta u$ and $u \gg \Delta u$.

410 4.2 Hertzian indenter

411 We now consider a Hertzian indenter as transferability test for our effective potential. In addition, the
 412 effects that thermal fluctuations have on the load displacement relation are explored along with an analysis
 413 of how to meaningfully define a contact area in the presence of thermal fluctuations.

414 The solution of the continuous displacement field has no dimensionless number if the contact radius a_c is
 415 taken to be the unit of length. However, $a_c/\Delta a$ starts to matter as soon as it is no longer large compared to
 416 unity. Since discreteness effects are a different topic discussed elsewhere [26], $a_c/\Delta a$ is chosen sufficiently
 417 large so that the discrete problem reflects the continuous Hertz contact reasonably well.

418 To test the applicability of the thermal repulsive-zone model in the realm of Hertzian contact mechanics,
 419 the following parameters were chosen as useful defaults after some trial and error: $R_c = 256 \Delta a$ and a
 420 normal load of $L = 131 E^* \Delta a^2$ leading to $a_c \approx 30 \Delta a$ within regular Hertzian contact mechanics. In the
 421 athermal Hertzian contact, the mean contact pressure turns for these parameters is $p \approx 0.049 E^*$. Results
 422 for the stress profile at a temperature of $k_B T = 0.2 E^* \Delta a^3$ are shown in Fig. 5.

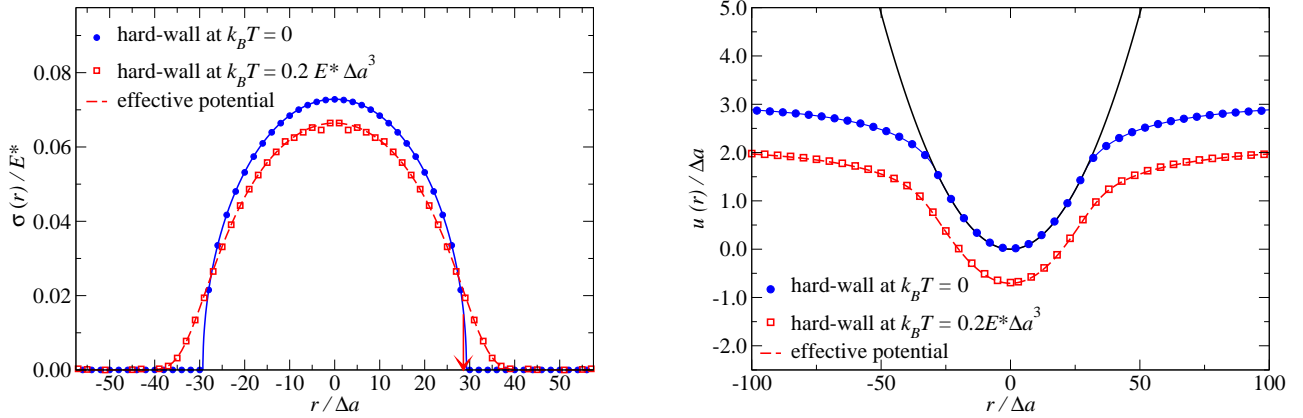


Figure 5. Left: Interfacial stress σ as a function of distance r from the symmetry axis in a Hertzian contact geometry. The (blue) circles reflect zero temperature data from the hard-wall overlap potential. The full (blue) line represents the analytical solution to the Hertz problem. The (red) open squares show finite-temperature data from full simulations, while the (red) dotted line shows zero-temperature simulations, in which, however, the effective potential was constructed to reflect thermal vibrations at the given temperature. The arrow marks the point of largest slope for the thermal indenter. **Right:** Displacement field $u(r)$ as a function of distance r from the symmetry axis.

423 An interesting but perhaps also obvious outcome of the data presented in Fig. 5 is that there is no abrupt
 424 transition from finite to zero contact stress, once thermal fluctuations are finite. This observations is of
 425 relevance when discussing the concept of “true contact area”. Since collisions in a hard-wall potential are
 426 instantaneous, the probability of observing two (finite) surfaces to be in contact has a statistical measure of
 427 zero, so that the instantaneous contact area could be argued to be (almost) always zero. Contact exists only
 428 in the isolated moments of time at which collisions take place. However, during these isolated moments of
 429 time, the forces between surfaces is infinitely large such that time averaging yields a distribution which
 430 resembles the well-known Hertzian stress profile; the smaller the temperature the closer the stress profiles
 431 between original and finite-temperature stress profiles.

432 The question of how to meaningfully define (repulsive) contact area when repulsion has a finite range and
 433 adhesion is neglected arises naturally. In a recent paper [26], it was proposed to define the contact line (or
 434 edge) to be located, where the gradient of the normal stress has a maximum slope. In the current example,
 435 this leads to a reduction of the contact radius of order 1%, which is significantly less than the reduction of
 436 approximately 30% of the normal displacement in the given case study.

437 In contrast to contact radii, force and displacement can be defined unambiguously. Thermal noise will
 438 reduce the interference d by d_T due to the effectively finite range of the repulsion, as discussed in the
 439 definition of the model in Sect. 2.1. Since the description for an athermal Hertzian contact is scale free—in
 440 the sense that the functional form for stress and displacement are independent of any parameter defining a
 441 Hertzian contact—the function $f(T) \equiv d_T/d_0$ must have a universal shape if $\Delta a \ll a_c$. This is because the
 442 thermal repulsive zone model for hard-wall repulsion is a scale-free function of the gap divided by Δu .
 443 Fig. 6 reveals that results on the thermal displacement for different Hertzian contact realizations can indeed
 444 be collapsed quite closely onto a single master curve $\Xi(T/\tilde{T})$ defined through

$$d_T = \tilde{d}_0 \Xi(T/\tilde{T}), \quad (64)$$

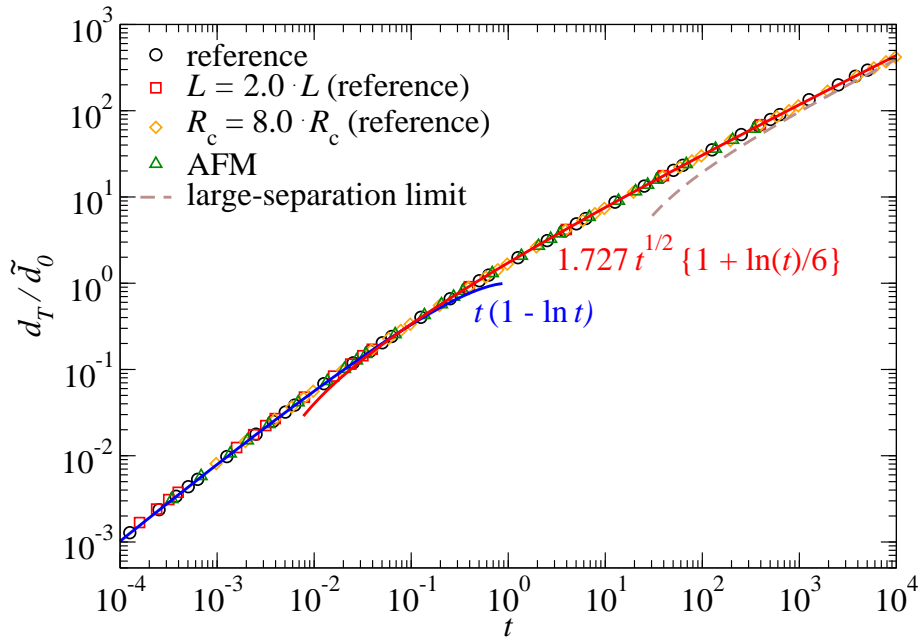


Figure 6. Reduced thermal displacement d_T/\tilde{d}_0 as a function of reduced temperature $t = T/\tilde{T}$ for different Hertzian contact realizations. The default model (black circles) is defined in the method section. In one case, load was increased by a factor of two (red squares), and in another case, the radius of curvature was increased by a factor of eight (orange diamonds) with respect to the default values. Finally, values found for blunt atomic-force microscope (AFM) tips were also considered: $\Delta a = 2.5 \text{ \AA}$, $R_c = 200 \text{ nm}$, $E^* = 100 \text{ GPa}$, and $L = 200 \text{ nN}$ (green triangles). Solid blue and red line show the low- and intermediate-temperature approximation from Eq. (67). The dashed brown line represents the high-temperature limit of Eq. (60).

445 where

$$\tilde{d}_0 = \left(\frac{R_c L}{E^* \Delta a^3} \right)^{-\frac{1}{3}} d_0 \tag{65}$$

446 and

$$\tilde{T} = \left(\frac{L}{E^* R_c^2} \right)^{\frac{2}{3}} \frac{E^* \Delta a^3}{k_B}. \tag{66}$$

447 The master curve shown in Fig. 6 reveals asymptotic regimes at low and at high temperatures, respectively.
 448 They can be approximated with power laws. However corrections logarithmic in temperature need to
 449 be made at low temperature to obtain quantitative agreement over broad temperature ranges. We find
 450 numerically that

$$\Xi(t) \approx \begin{cases} t(1 - \ln t) & \text{for } t \ll 1 \\ 1.727 \sqrt{t} \{1 + \ln(t)/6\} & \text{for } 0.1 < t < 10^4 \end{cases} \quad (67)$$

451 Inserting the low-temperature approximation of the master curve into Eq. (64) and reshuffling terms
 452 yields

$$\frac{d_T}{d_0} \approx \frac{T}{T^*} \left(1 - \ln \frac{T}{\tilde{T}} \right) \quad (68)$$

453 for $T \ll \tilde{T}$. This means that the low-temperature treatment presented in Sect. 3.3.2 obtained the correct
 454 linear term, but failed to predict the logarithmic corrections, which become very large at small ratios
 455 T/\tilde{T} . Before discussing the origin of those corrections, we wish to emphasize that there are indeed two
 456 characteristic temperatures for the Hertzian contact, namely T^* and \tilde{T} .

457 The suspicion that significantly better results at small T/\tilde{T} are obtained when extending the integration
 458 domain in Eq. (52) back to radii beyond the athermal contact radius turns out incorrect. The main reason for
 459 the deviations lies in the assumption of a constant thermal shift of the thermal displacement. Fig. 7 reveals
 460 that the thermal shift far away from the indenter is noticeably larger than at $r = 0$ and that discrepancies
 461 grow (logarithmically) with decreasing temperature. Since the simple treatment allows one to rationalize
 462 why d_T is (roughly) linear in temperature, we decided to keep the discussion of the low-temperature limit.

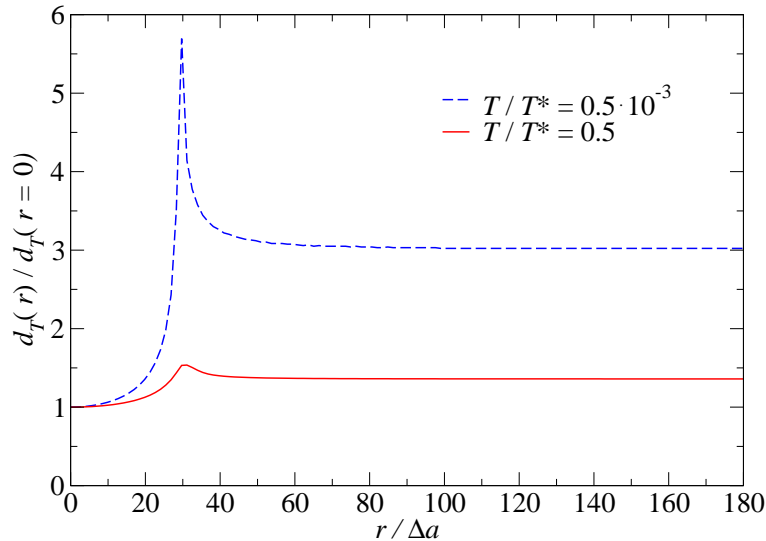


Figure 7. Spatially resolved thermal displacement $d_T(r)$ normalized to its value at $r = 0$ at two different reduced temperatures T/T^* for the default model. Lower and upper temperature are indicated by dashed blue and solid red lines, respectively.

463 Before investigating the magnitude of thermal displacements in real units and not just in reduced units,
 464 we briefly comment on the intermediate-temperature behavior. Most importantly, we wish to emphasize
 465 that the approximation made in Eq. (67) for $t > 0.1$ is only valid on the shown domain and that it does
 466 *not* extend to $t \rightarrow \infty$. However, from a practical point of view, it appears virtually impossible to design
 467 a real-laboratory experiment, in which the asymptotic high-temperature regime of $t > 10^3$ could ever
 468 be reached. The only possible exception coming to our minds would involve the use of hagfish slime.
 469 It has extraordinarily small elastic moduli of order 0.02 Pa [27], though the values of Δa to be used in
 470 a continuum model would be clearly in excess of the atomic scale, because hagfish slime stops being
 471 homogeneous well above the atomic scale. Since the contact mechanics of hagfish slime and related
 472 systems is somewhat of a niche application, we would argue that the analytical solution given in Eq. (60) is
 473 merely a nice mathematical result and that the $t > 0.1$ approximation made in Eq. (67) can be considered
 474 the high-temperature limit for all other purposes.

475 One may wonder how the master curve shown in Fig. 6 translates into a $d(T)$ dependence when real
 476 units rather than reduced units are used. To answer that question, the expansions obtained previously are
 477 represented again for a moderately hard-matter ($E^* = 1$ GPa) and a soft-matter ($E^* = 50$ MPa) system,
 478 see Fig. 8 and further validated by additional GFMD simulations. In both cases, a radius of curvature of
 479 $R_c = 50$ nm was assumed and the load was chosen such that the ratio of maximum Hertz pressure to E^*
 480 was in the order of 0.1%, i.e., a load where plastic deformation can be assumed to be minor.

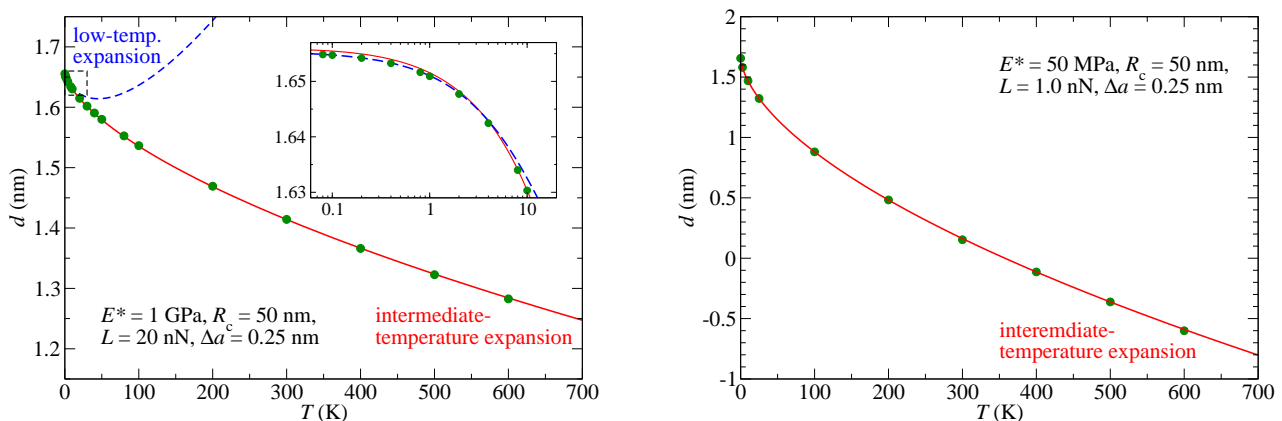


Figure 8. Displacement as a function of temperature at fixed load for a moderately hard-matter (**left**, $E^* = 1$ GPa) and a soft-matter (**right**, $E^* = 50$ MPa) system. Symbols indicate the results from GFMD simulations, while blue and red lines represent the low-temperature and intermediate-temperature approximations, respectively.

481 Fig. 8 reveals that both studied systems qualify as being clearly in the intermediate-temperature regime at
 482 room temperature. Relative corrections of the normal displacement for the stiffer system are rather minor
 483 but non-negligible for the soft-matter system. This observation brings us to the next and final question,
 484 which is addressed in Fig. 9, namely to what extent do thermal correction affect the load-displacement
 485 relation? After all, most indentation experiments are done at constant temperature and varying load rather
 486 than at constant load and varying temperature. Combining Eqs. (??–66) with the intermediate-temperature
 487 expansion of Eq. (67) and the analytical solution for the displacement-load relation in a Hertzian contact,

488 leads to the following relation:

$$d_T = d_T^{\text{ref}} \left\{ 1 - \frac{1}{9} \ln \left(L/L^{\text{ref}} \right) \right\} \quad (69)$$

489 with $d_T^{\text{ref}} \approx 1.426 \Delta u$ and

$$L^{\text{ref}} = \left(\frac{k_B T}{E \Delta a^3} \right)^{3/2} E^* R_c^2. \quad (70)$$

490 In other words, the elastomer surface is effectively shifted by a little less than 1.5 times the thermal standard
 491 deviation of its smallest-scale surface fluctuations. The effects of load are minuscule as they enter only
 492 logarithmically in the ninth' root of the load.

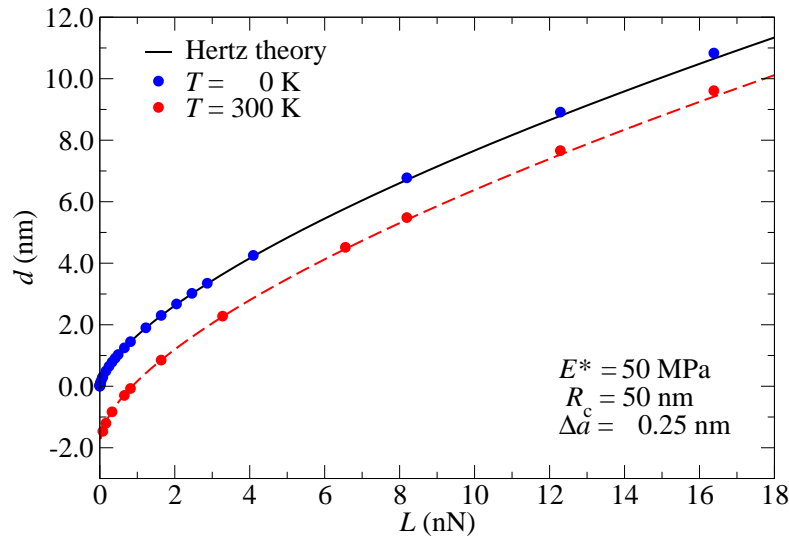


Figure 9. Displacement as a function of load at zero and room temperature for a moderately hard-matter for a soft-matter ($E^* = 50$ MPa) system. Symbols indicate the results from GFMD simulations, while blue and red lines represent the low-temperature and intermediate-temperature approximations, respectively.

493 Fig. 9 confirms that the thermal fluctuation in most real Hertzian contacts should lead to corrections that
 494 appear as almost constant shifts to the eye, even for soft-matter systems, for which the absolute shifts
 495 can be relatively large. In the case study presented in Fig. 9, the thermal shift reads $d_T \approx 1.2$ at a load
 496 of $L \approx 16$ nN and barely more at a much reduced load $d_T \approx 1.7$ at a load as small as $L \approx 0.16$ nN In
 497 order for the d_T correction to acquire twice the value compared to that at 16 nN, the compressive force
 498 in our example would have to be as small as $L \approx 20$ fN, which is scarcely measurable. For the reasons
 499 of completeness, we state that the range of validity of the intermediate-temperature approximation of
 500 $0.1 < t < 10^4$ demonstrated in Fig. 6 translates to a range of loads of $0.15 < L/\text{nN} < 1.5 \cdot 10^4$ for the
 501 specific examples studied here. Upper and lower limits are well beyond loads that could be meaningfully
 502 applied or measured experimentally for the system of question while measuring the normal displacement
 503 with high resolution.

5 SUMMARY

504 In this work, we analyzed the effect that thermal fluctuations can have on contact mechanics in the case of
505 hard-wall interactions. To this end, we first demonstrated that thermal surface fluctuations are dominated
506 by short wavelengths undulations. They smear out the originally infinitesimally short-range repulsion to a
507 finite range of $\Delta u \approx \sqrt{k_B T / (E^* \Delta a)}$. The functional form of the repulsive force was derived analytically
508 and shown to diverge inversely proportionally with the interfacial separation u_0 at small u_0 but to decay
509 slightly more quickly than exponentially in $-u_0^2$ at separations clearly exceeding Δu .

510 To come to these results, the Green's function molecular dynamics (GFMD) technique was generalized
511 to include thermal noise. Particular emphasis was placed on the question how to handle (the original)
512 hard-wall interactions in the simulations. We found that replacing the hard-wall overlap constraint with
513 a stiff harmonic potential produces satisfactory results if simulations are done at different values for the
514 stiffness and extrapolation is made to infinite stiffness. The GFMD results are described very well with
515 different mean-field approximations to the problem, which made it possible to identify a highly-accurate,
516 closed-form analytical expression for the distance-force relation in a flat, thermal elastomer on a flat, rigid
517 substrate configuration.

518 It may be important to note that each microscopic interaction law requires the coarse-graining to be done
519 for that particular interaction. For example, if thermal fluctuations were to be treated in a Dugdale model,
520 results for the hard-wall constraint cannot be simply incorporated, but a new parametrization of thermal
521 effects has to be done.

522 Application of our methodology to Hertzian contacts revealed that thermal fluctuations can induce non-
523 negligible shifts in the normal displacement. However, corrections turn out to depend only logarithmically
524 on the ninth' root of the normal load. This result may, in part, explain why Hertzian contact models often
525 apply all the way down to the nanoscale: Essentially constant shifts remain unnoticed.

526 As a zero-order approximation, it can be assumed that the thermally induced shift of a Hertzian indenter
527 is a little less than 1.5 times the thermal standard deviation of surface positions of a free, unconstrained
528 surface. This result is relatively insensitive to the radius of curvature of the Hertzian indenter, which is
529 why we expect similar results for randomly rough and other hard-wall indenters. However, the effect of
530 thermal fluctuations will be more important in the case of short-range adhesion. Given the results from
531 this study, quite noticeable effects may be expected when the range of adhesion is in the order of or less
532 than the thermal displacement Δu . Future studies are ongoing elucidating the reduction of adhesion due to
533 thermal vibrations.

REFERENCES

- 534 [1]Binquan Luan and Mark O. Robbins. The breakdown of continuum models for mechanical contacts.
535 *Nature*, 435(7044):929–932, jun 2005.
- 536 [2]Binquan Luan and Mark O. Robbins. Contact of single asperities with varying adhesion: Comparing
537 continuum mechanics to atomistic simulations. *Physical Review E*, 74(2):026111, aug 2006.
- 538 [3]Yifei Mo, Kevin T. Turner, and Izabela Szlufarska. Friction laws at the nanoscale. *Nature*,
539 457(7233):1116–1119, February 2009.
- 540 [4]Shengfeng Cheng, Binquan Luan, and Mark O. Robbins. Contact and friction of nanoasperities: Effects
541 of adsorbed monolayers. *Physical Review E*, 81(1):016102, January 2010.
- 542 [5]Yifei Mo and Izabela Szlufarska. Roughness picture of friction in dry nanoscale contacts. *Physical*
543 *Review B*, 81(3):035405, January 2010.

- 544 [6]S Eder, A Vernes, G Vorlauffer, and G Betz. Molecular dynamics simulations of mixed lubrication with
545 smooth particle post-processing. *Journal of Physics: Condensed Matter*, 23(17):175004, April 2011.
- 546 [7]Tevis D. B. Jacobs and Ashlie Martini. Measuring and understanding contact area at the nanoscale: A
547 review. *Applied Mechanics Reviews*, 69(6):060802, November 2017.
- 548 [8]A. V. Pinon, M. Wiercz-Kien, A. D. Craciun, N. Beyer, J. L. Gallani, and M. V. Rastei. Thermal effects
549 on van der waals adhesive forces. *Physical Review B*, 93(3), January 2016.
- 550 [9]Tian Tang, Anand Jagota, Manoj K. Chaudhury, and Chung-Yuen Hui. Thermal fluctuations limit the
551 adhesive strength of compliant solids. *The Journal of Adhesion*, 82(7):671–696, June 2006.
- 552 [10]Josep C. Pàmies, Angelo Cacciuto, and Daan Frenkel. Phase diagram of Hertzian spheres. *The Journal*
553 *of Chemical Physics*, 131(4):044514, July 2009.
- 554 [11]M.P. Allen and D.J. Tildesley. *Computer Simulation of Liquids*. Clarendon, Oxford, 1987.
- 555 [12]Daan Frenkel and Berend Smit. *Understanding Molecular Simulation: From Algorithms to*
556 *Applications*, volume 1 of *Computational Science Series*. Academic Press, San Diego, second
557 edition, 2002.
- 558 [13]I.A. Polonsky and L.M. Keer. A numerical method for solving rough contact problems based on the
559 multi-level multi-summation and conjugate gradient techniques. *Wear*, 231(2):206–219, July 1999.
- 560 [14]M. H. Müser, W. B. Dapp, R. Bugnicourt, P. Sainsot, N. Lesaffre, T. A. Lubrecht, B. N. J. Persson,
561 K. Harris, A. Bennett, K. Schulze, S. Rohde, P. Ifju, W. G. Sawyer, T. Angelini, H. Ashtari Esfahani,
562 M. Kadkhodaei, S. Akbarzadeh, J.-J. Wu, G. Vorlauffer, A. Vernes, S. Solhjoo, A. I. Vakis, R. L.
563 Jackson, Y. Xu, J. Streater, A. Rostami, D. Dini, S. Medina, G. Carbone, F. Bottiglione, L. Afferrante,
564 J. Monti, L. Pastewka, M. O. Robbins, and J. A. Greenwood. Meeting the contact-mechanics challenge.
565 *Tribology Letters*, 65(4), aug 2017.
- 566 [15]Carlos Campaña and Martin H. Müser. Practical Green’s function approach to the simulation of elastic
567 semi-infinite solids. *Phys. Rev. B*, 74(7):075420, aug 2006.
- 568 [16]Yunong Zhou, Michael Moseler, and Martin H. Müser. Solution of boundary-element problems using
569 the fast-inertial-relaxation-engine method. *Physical Review B*, 99(14), April 2019.
- 570 [17]Martin H Müser. Single-asperity contact mechanics with positive and negative work of adhesion:
571 Influence of finite-range interactions and a continuum description for the squeeze-out of wetting fluids.
572 *Beilstein J. Nanotechnol.*, 5:419–437, apr 2014.
- 573 [18]B. Derjaguin. Untersuchungen über die Reibung und Adhäsion, IV. *Kolloid-Zeitschrift*, 69(2):155–164,
574 November 1934.
- 575 [19]Ryogo Kubo. Statistical-mechanical theory of irreversible processes. i. general theory and simple
576 applications to magnetic and conduction problems. *Journal of the Physical Society of Japan*, 12(6):570–
577 586, June 1957.
- 578 [20]Seiji Kajita, Hitoshi Washizu, and Toshihide Ohmori. Approach of semi-infinite dynamic lattice
579 Green’s function and energy dissipation due to phonons in solid friction between commensurate
580 surfaces. *Physical Review B*, 82(11):115424, September 2010.
- 581 [21]Seiji Kajita. Green’s function nonequilibrium molecular dynamics method for solid surfaces and
582 interfaces. *Physical Review E*, 94(3):033301, September 2016.
- 583 [22]Jan Steven van Dokkum and Lucia Nicola. Green’s function molecular dynamics including
584 viscoelasticity. *Modelling and Simulation in Materials Science and Engineering*, 27(7):075006,
585 August 2019.
- 586 [23]Xuejuan Xu, Anand Jagota, and Chung-Yuen Hui. Effects of surface tension on the adhesive contact
587 of a rigid sphere to a compliant substrate. *Soft Matter*, 10(26):4625–4632, 2014.

- 588 [24]Bruce J. Berne and D. Thirumalai. On the simulation of quantum systems: Path integral methods.
589 *Annual Review of Physical Chemistry*, 37(1):401–424, October 1986.
- 590 [25]Herbert A David and Haikady N Nagaraja. *Order Statistics. 2003*. Wiley, New York, 2003.
- 591 [26]Martin H. Müser. Elasticity does not necessarily break down in nanoscale contacts. *Tribol. Lett.*, 67:57,
592 jun 2019.
- 593 [27]Randy H. Ewoldt, Timothy M. Winegard, and Douglas S. Fudge. Non-linear viscoelasticity of hagfish
594 slime. *International Journal of Non-Linear Mechanics*, 46(4):627–636, May 2011.